



**HAL**  
open science

# A three-dimensional seismic tomographic study of the gas hydrate stability zone, offshore Vancouver Island

J. W. D. Hobro, T. A. Minshull, S. C. Singh, S. Chand

► **To cite this version:**

J. W. D. Hobro, T. A. Minshull, S. C. Singh, S. Chand. A three-dimensional seismic tomographic study of the gas hydrate stability zone, offshore Vancouver Island. *Journal of Geophysical Research: Solid Earth*, 2005, 110, pp. 639-646. 10.1029/2004JB003477 . insu-03601110

**HAL Id: insu-03601110**

**<https://insu.hal.science/insu-03601110>**

Submitted on 8 Mar 2022

**HAL** is a multi-disciplinary open access archive for the deposit and dissemination of scientific research documents, whether they are published or not. The documents may come from teaching and research institutions in France or abroad, or from public or private research centers.

L'archive ouverte pluridisciplinaire **HAL**, est destinée au dépôt et à la diffusion de documents scientifiques de niveau recherche, publiés ou non, émanant des établissements d'enseignement et de recherche français ou étrangers, des laboratoires publics ou privés.

Copyright

## A three-dimensional seismic tomographic study of the gas hydrate stability zone, offshore Vancouver Island

J. W. D. Hobro,<sup>1</sup> T. A. Minshull,<sup>2</sup> S. C. Singh,<sup>3</sup> and S. Chand<sup>2,4</sup>

Received 13 October 2004; revised 17 May 2005; accepted 17 June 2005; published 14 September 2005.

[1] Methane hydrate bottom-simulating reflectors (BSRs) are widespread on the northern Cascadia margin offshore Vancouver Island. We conducted a three-dimensional tomographic seismic study of the hydrate stability zone in an area around Ocean Drilling Program Site 889 using two deployments of five ocean bottom hydrophones and air gun shots along a series of closely spaced profiles in various orientations. Further constraints on reflector geometry come from coincident single-channel reflection profiles. Travel times of reflected and refracted phases were inverted with a regularized three-dimensional inversion using perturbation ray tracing through smooth isotropic media for the forward step. The seismic data allow us to constrain the velocity structure in a  $\sim 6 \text{ km}^2$  area around the drill site. Mean velocities range from  $1.50 \text{ km s}^{-1}$  at the seabed to  $1.84 \text{ km s}^{-1}$  at the BSR, and velocities at Site 889 match well those measured using a vertical seismic profile. At equivalent depths below the seafloor, velocities vary laterally by typically  $\sim 0.15 \text{ km s}^{-1}$ . Close to the seafloor, velocities may be controlled primarily by lithology, but close to the BSR we infer hydrate contents of up to 15% of the pore space from effective medium modeling. The mean hydrate saturation in the well-constrained volume of the velocity model is estimated to be 2.2%. There is no correlation between the seismic velocity above the BSR and the reflection coefficient at the BSR, so the latter is likely controlled primarily by the distribution of free gas beneath the hydrate stability zone.

**Citation:** Hobro, J. W. D., T. A. Minshull, S. C. Singh, and S. Chand (2005), A three-dimensional seismic tomographic study of the gas hydrate stability zone, offshore Vancouver Island, *J. Geophys. Res.*, 110, B09102, doi:10.1029/2004JB003477.

### 1. Introduction

[2] Methane hydrates are formed in continental margin sediments where sufficient methane is present to saturate the pore water and the pressure and temperature fall within the hydrate stability field. Typically these conditions are satisfied in the top few hundred meters of the sediment column and at water depths greater than a few hundred meters. Quantification of gas hydrate in such sediments is important because of their resource potential and their potential impact on global climate change. Hydrates are most commonly quantified using seismic measurements [e.g., Lee *et al.*, 1996; Ecker *et al.*, 2000; Chand *et al.*, 2004]. International efforts using seismic methods and direct sampling to understand continental margin gas hydrate systems have focused on several specific sites. One of these sites is the Vancouver Island margin, where drilling on Ocean Drilling Program (ODP) Leg 146 [Westbrook *et al.*, 1994] has been complemented by multichannel, single channel, and high-

resolution deep-towed seismic reflection surveys [e.g., Hyndman and Spence, 1992; Fink and Spence, 1999; Riedel *et al.*, 2002; Wood *et al.*, 2002; Chapman *et al.*, 2002; Zühlsdorff and Spiess, 2004], controlled source electromagnetic surveys [Yuan and Edwards, 2000], and direct seafloor sampling [Riedel *et al.*, 2002, 2005].

[3] At the Vancouver Island margin, a 4-km-thick sediment column overlying the subducting Juan de Fuca plate is accreted to the North American plate and deformed by a series of folds and thrusts [e.g., Westbrook *et al.*, 1994]. Within the accreted sediments, seismic reflection data have revealed a widespread, high amplitude bottom simulating reflector (BSR) marking the base of the hydrate stability zone. At ODP Site 889 (Figure 1a), the BSR was penetrated and a vertical seismic profile confirmed that this reflector marks the boundary between hydrate-bearing sediments and a region of free gas [MacKay *et al.*, 1994]. Surface and deep-towed reflection data have shown the presence of a series of “blank” zones within the hydrate stability field interpreted as possible vent sites, and piston coring at some of these sites has recovered hydrate at the seafloor [Wood *et al.*, 2002; Riedel *et al.*, 2002]. Deep-towed reflection data also have revealed significant small-scale roughness of the BSR that is not resolved in surface seismic data [Wood *et al.*, 2002]. Velocity analyses of multichannel seismic data indicate that substantial *P* wave velocity anomalies are present within the hydrate stability field [e.g., Yuan *et al.*,

<sup>1</sup>WesternGeco, Gatwick, UK.

<sup>2</sup>Southampton Oceanography Centre, Southampton, UK.

<sup>3</sup>Laboratoire de Géosciences Marines, Institut de Physique du Globe de Paris, Paris, France.

<sup>4</sup>Now at Geological Survey of Norway, Tromsø, Norway.

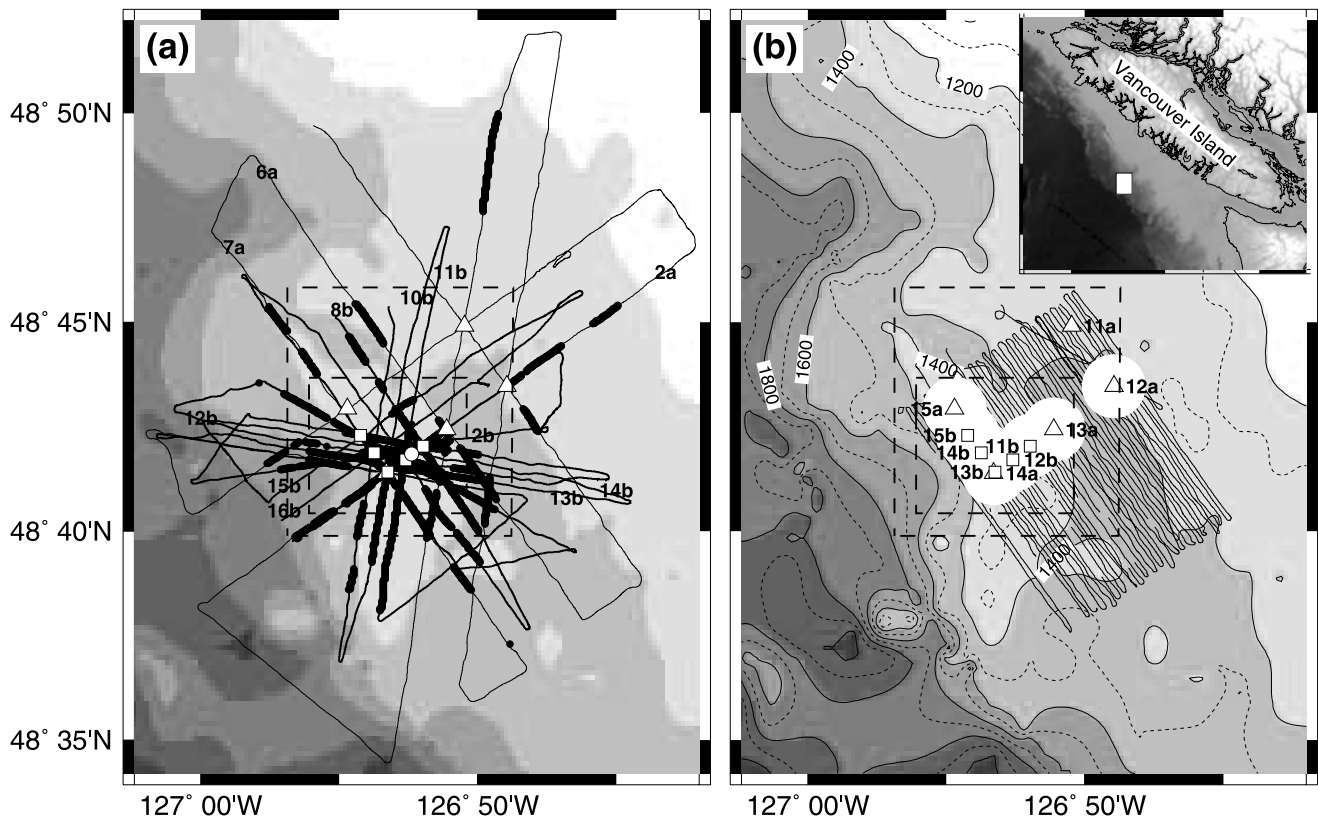


**Figure 1.** (a) Layout of OBH experiment. Grey scale marks bathymetry, with darker shades marking deeper water. Thin solid line marks shooting track during first OBH deployment, with triangles marking OBH positions. Thicker line marks shooting track during second OBH deployment, with squares marking OBH positions. Overlapping solid circles mark portions of the shooting track where BSR picks were made in coincident reflection profiles. Circle marks ODP Site 889. Profiles from which data are shown elsewhere in the paper are labeled. (b) Bathymetry marked as in Figure 1a but here also contoured at 100-m intervals. White circles around instrument positions mark approximately the regions where sediment velocities are constrained by refracted arrivals. Solid line marks shooting track for detailed reflection survey. Outer box marks region chosen for tomographic inversion; inner box marks well-constrained region chosen for the final run of the inversion.

1996]. These velocity anomalies have been interpreted to indicate relatively large hydrate contents in the lower part of the stability field, with estimated hydrate saturations of up to 20–30% of the pore space [Hyndman *et al.*, 2001]. A reconnaissance controlled source electromagnetic survey found little difference in resistivity between areas where a BSR is present and areas without a BSR, suggesting that hydrate is ubiquitous in the region [Yuan and Edwards, 2000].

[4] In terms of hydrate quantification, seismic reflection studies are limited by the relatively poor constraints that are provided on long-wavelength velocity variations. Hence the same multichannel seismic data set has been used to argue that the impedance contrast at the bottom simulating reflector (BSR) offshore Vancouver Island is due primarily to the presence of gas beneath the BSR [Singh *et al.*, 1993], and that it is due primarily to the presence of hydrate above the BSR [Yuan *et al.*, 1996]. The long-wavelength component of subsurface seismic velocity variations is best resolved using wide-angle seismic data recorded on the ocean floor [e.g., Katzman *et al.*, 1994; Korenaga *et al.*, 1997]. A detailed seismic study of the region around ODP Site 889 was conducted in 1993 using 1.97-L (120 cubic inches) and

0.65-L (40 cubic inches) sources, a single-channel streamer and five ocean bottom hydrophones (OBHs) deployed twice in different configurations (Figure 1). A preliminary analysis of these data was presented by Spence *et al.* [1995]. Fink and Spence [1999] presented a detailed analysis of the seismic reflection data, Hobro *et al.* [1998] presented analyses of a two-dimensional subset of the wide-angle data, and Hobro *et al.* [2003] used part of the three-dimensional data set to illustrate their tomographic inversion method. Here we present an analysis and interpretation of the full OBH data set using three-dimensional seismic tomography and effective medium theory. Our tomographic method is isotropic and involves perturbation ray tracing through smooth media for the forward step and conjugate gradients for the inverse step; further details are given by Hobro [1999].

## 2. Seismic Data

[5] In the vicinity of Site 889, the BSR occurs typically 200–250 m below the seafloor. In the hydrate stability zone above the BSR, the vertical velocity gradient is typically rather high, with velocities increasing from  $\sim 1.5 \text{ km s}^{-1}$

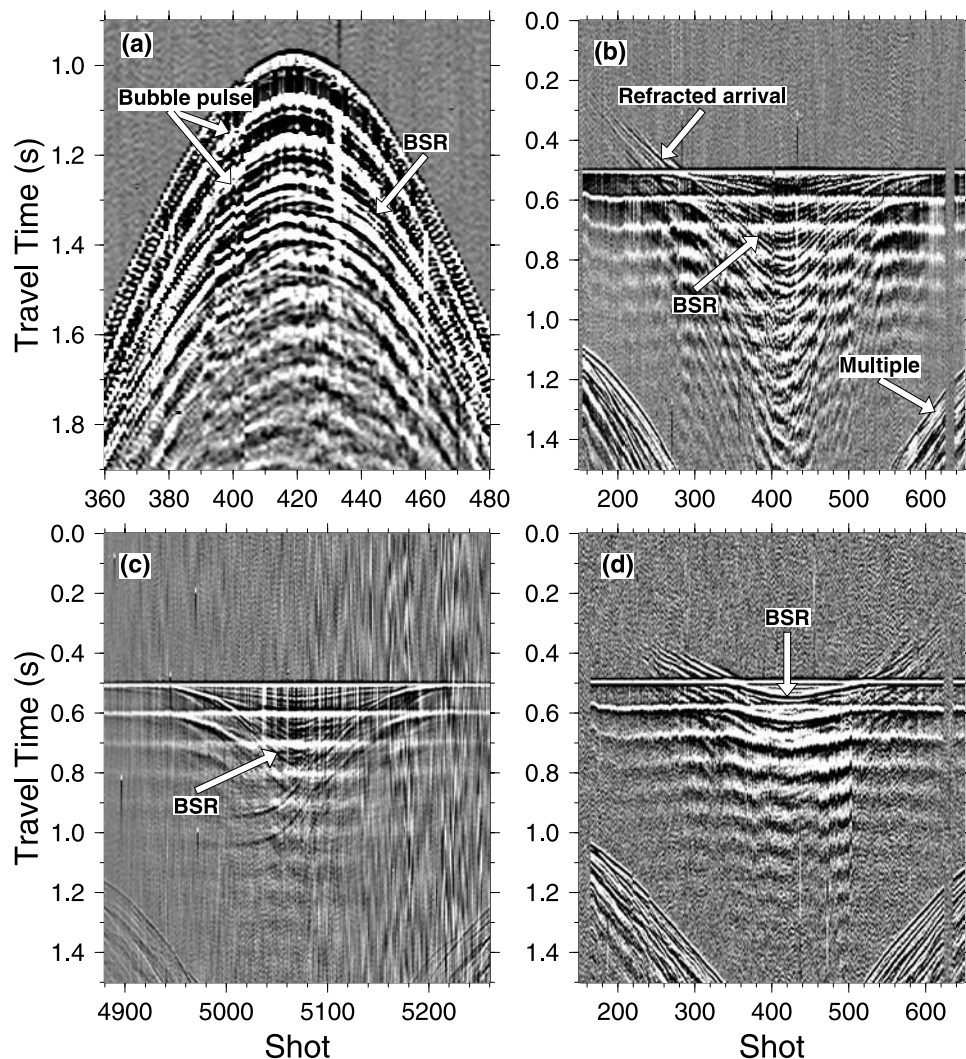


**Figure 2.** Representative OBH record sections. (a) Unreduced data from OBH12, deployment A. BSR is difficult to identify due to interfering bubble pulses from the direct arrival and to noise. (b) In-line data from OBH12, deployment A displayed with the direct arrival flattened. Strong BSR reflections are visible, and refracted energy both before and after the direct arrival. (c) In-line data from OBH14, deployment A, with a very weak BSR. (d) Off-line data from OBH13, deployment A showing a strong refracted energy before and after the direct arrival.

close to the seafloor to perhaps as much as  $\sim 1.9 \text{ km s}^{-1}$  just above the BSR [Yuan *et al.*, 1996]. Therefore rays turn rapidly within the hydrate stability zone, and to obtain good velocity constraints, a relatively short receiver spacing is required. Given that only five instruments were available for the experiment, OBHs were deployed in two configurations, with a spacing of 3.3 km in the first deployment (deployment A) and 1 km in the second deployment (deployment B). Wide-angle data were acquired primarily with the 1.97-L air gun, with the smaller gun used only on part of one profile when the larger gun failed. The nominal shot spacing was 35 m. OBHs were programmed with their minimum sample interval of 4 ms. Unfortunately, for many OBH/profile pairs the direct water wave arrivals were clipped, so standard processing steps such as bandpass filtering and predictive deconvolution could not be applied without generating significant artifacts. All record sections exhibit strong bubble pulses; however, the BSR is clearly

visible around 300 ms after the direct arrival when data are displayed with the direct arrival “flattened” to constant two-way time (Figure 2). The data quality was therefore perfectly adequate for the travel time tomography described below, but not good enough for detailed waveform analysis. In some record sections, significant energy turning in the steep velocity gradient was observed crossing the direct arrival to become a first arrival beyond  $\sim 4$ -km source-receiver range.

### 3. Source and Receiver Relocation

[6] Shot and receiver locations were determined initially from Global Positioning System (GPS) navigation, which was logged without differential corrections. However, the  $\sim 100 \text{ m}$  uncertainty in these positions resulting from selective availability is potentially an important source of error in velocities determined by tomographic inversion.

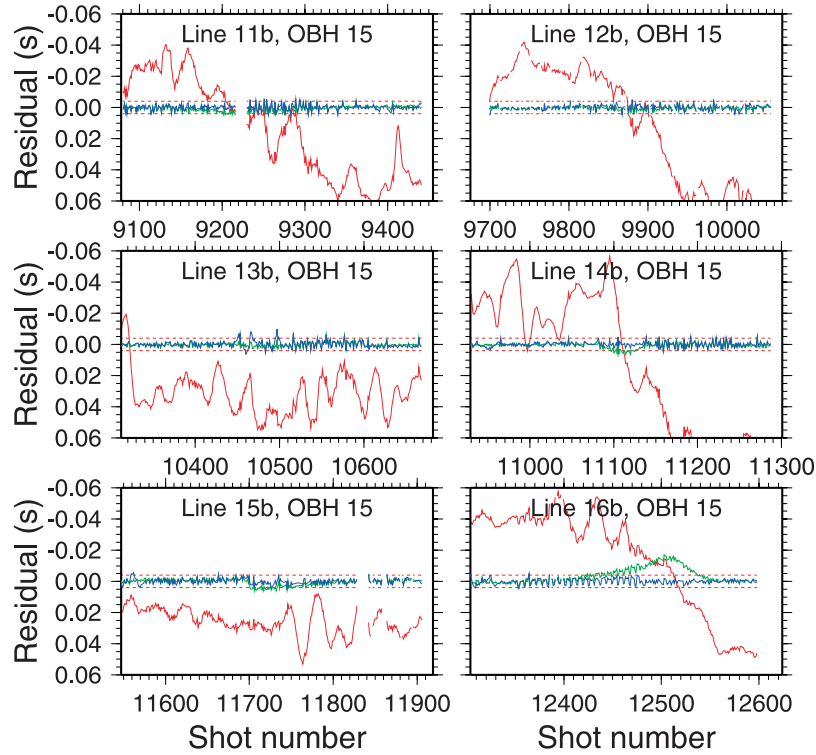


**Figure 3.** A selection of data and residuals for shot and instrument relocation, for the second OBH deployment. Travel time misfits are shown for the starting model (red), the model resulting from shot and instrument relocation (green), and the model resulting from a relocation algorithm in which static time shifts are also allowed (blue). Dashed lines show pick uncertainties.

The OBH data set contains detailed constraints on the shot and receiver positions in the form of the travel times of signals travelling directly through the water column to the instruments. Travel times for these arrivals were picked and assigned an uncertainty of 4–8 ms, depending on the signal-to-noise ratio. Ray tracing through a water column velocity structure based on conductivity-temperature-depth profiles showed that, for the purposes of modeling direct arrivals out to the maximum range recorded during the survey, the water velocity could be adequately approximated with a constant value of  $1.482 \pm 0.002 \text{ km s}^{-1}$ . Shot and receiver positions were refined using the inversion algorithm of *Hobro et al.* [2003] modified such that the velocity is fixed and constant but shot and receiver positions are allowed to vary. Initially the following functional was minimized:

$$\mathbf{F}(\delta\mathbf{m}) = \|\mathbf{r} - \mathbf{A}\delta\mathbf{m}\|_{\mathbf{D}}^2, \quad (1)$$

where  $\delta\mathbf{m}$  is a change in the model vector,  $\mathbf{r}$  is a travel time residual vector and  $\mathbf{A}$  is a matrix of Fréchet derivatives. The model vector consists of two horizontal coordinates and a depth for receivers, and two horizontal coordinates only for the source. The norm  $\|\cdot\|_{\mathbf{D}}$  is characterized by the inverse covariance matrix with diagonal components of  $1/\sigma_i^2$ , where  $\sigma_i$  is the uncertainty in the  $i$ th measured travel time, and off-diagonal components of zero. The contributions of shot and instrument coordinates to the misfit functions were normalized by the root-mean-square value of the components of  $\mathbf{A}$  for each parameter. Shot depths were assumed to be known and were fixed at 6 m during the inversion.

[7] An initial inversion for deployment A instrument positions only used 15 parameters (5 OBHs  $\times$  3 coordinates for each) and 16,950 picks, and reduced the  $\chi^2$  (normalized misfit) value from 88.1 to 20.5. In the second inversion run, deployment A shot positions were also allowed to vary, and the  $\chi^2$  value was reduced to 0.58. As a function of shot number, initial residuals contained a long-wavelength component due to errors in instrument position, a medium-wavelength (20–50 shots) component due to GPS drift, and a short-wavelength (1–5 shots) component due to random errors in timing and travel time picking (Figure 3). The inversion successfully removed the first two components, with the exception of a small element of longer-wavelength misfit that could be due to inadequate clock drift corrections (see below). However, this inversion resulted in large changes in shot positions which were poorly constrained, and shot spacings that would imply unreasonably large speeds and accelerations for the ship.

[8] Since the shot interval was constant in time, the distance between shots is expected to change only gradually, and the curvature of the shot track should be small. This constraint may be expressed mathematically as a minimization of the acceleration of the ship,

$$\frac{d^2\mathbf{x}}{dt^2} = \left( \frac{d^2x}{dt^2}, \frac{d^2y}{dt^2} \right), \quad (2)$$

where  $\mathbf{x}(t) = (x(t), y(t))$  is the ship's position as a function of time. The shot position is simply the ship's position plus an offset which is constant along each line of the survey. If

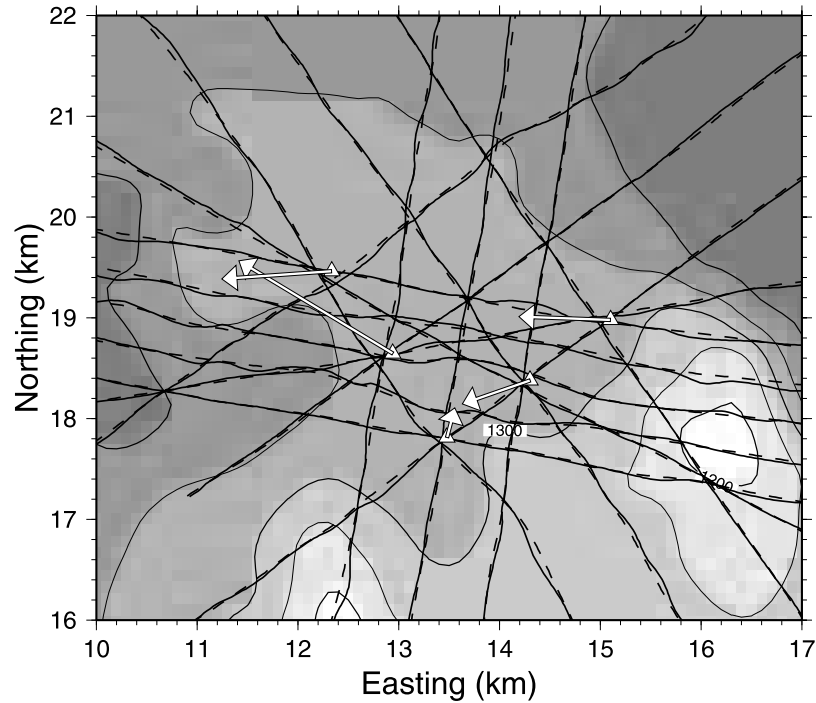


**Figure 4.** Original shot positions (thick solid lines mark) and relocated positions (dashed lines) for the second OBH deployment, shown here in the Cartesian reference frame of the tomographic model. Open triangles mark relocated ocean bottom seismometer positions, and arrows point toward the original (deployment) positions. Arrow length is 20 times true distance between original and relocated positions. Grey scale and contours mark bathymetry from seabed inversion.

consecutive shots are numbered ( $n, n + 1, n + 2, \dots$ ) and shots are spaced equally in time then

$$\frac{dn}{dt} = \text{const}, \quad (3)$$

so the acceleration of the ship is proportional to the quantity

$$\frac{d^2\mathbf{x}}{dn^2} = \left( \frac{d^2x}{dn^2}, \frac{d^2y}{dn^2} \right). \quad (4)$$

The standard least squares functional of equation (1) may be replaced by the regularized least squares functional

$$\mathbf{F}(\delta\mathbf{m}) = \|\mathbf{r} - \mathbf{A}\delta\mathbf{m}\|_{\mathbf{D}}^2 + \lambda \|\mathbf{m} + \delta\mathbf{m}\|_{\mathbf{M}}^2, \quad (5)$$

where the norm  $\|\cdot\|_{\mathbf{M}}$  is constructed to measure the quantity  $d^2\mathbf{x}/dn^2$  along each line in the survey and the parameter  $\lambda$  determines the strength of the regularization. In the final regularized inversion used for both deployments, a static travel time shift was also permitted for each profile/instrument pair, since clock drifts were sometimes large and may be poorly represented by linear interpolation between predeployment and postdeployment offsets. This inversion led to final  $\chi^2$  values of 0.12 for deployment A and 0.15 for deployment B, and successfully removed all but the short-wavelength picking errors (Figure 3). The regularization ensures that the shooting tracks are somewhat straighter than those produced by the raw GPS navigation (Figure 4). The very low  $\chi^2$  value achieved, despite fairly strong

regularization, suggests that travel time uncertainties for the direct arrival were overestimated by a factor of 2–3.

#### 4. Data Analysis

[9] Technical details of our regularized travel time inversion approach and its application to this data set are given by *Hobro et al.* [2003] and *Hobro* [1999]. The first step in the data analysis was to construct an accurate model of the seafloor within the survey area, since the bathymetry was not adequately constrained by existing data. A seabed model was constructed using single-channel reflection data acquired at the same time as the wide-angle data and relocated shot positions; the single-channel grids of *Fink and Spence* [1999] were not used because for these profiles the shot positions were not sufficiently accurate and could not be relocated. Seabed reflection travel time picks were typically assigned an uncertainty of 3 ms. The seabed was parameterized as a 100 by 100 grid covering a rectangular area of 25 km by 29 km, and the water depth determined using the regularized inversion with the water velocity kept constant as above. This inversion is effectively a map migration of the seabed. Separate inversions were carried out for each of the two OBH deployments, since the shot and receiver relocation gives only relative, not absolute positions, and so after relocation there may be an undetermined offset in absolute position between the two deployments. Two well-constrained perpendicular profiles were chosen that were shot during both deployments and the horizontal offset between these tracks determined by maximizing the correlation between the resulting seabed pro-

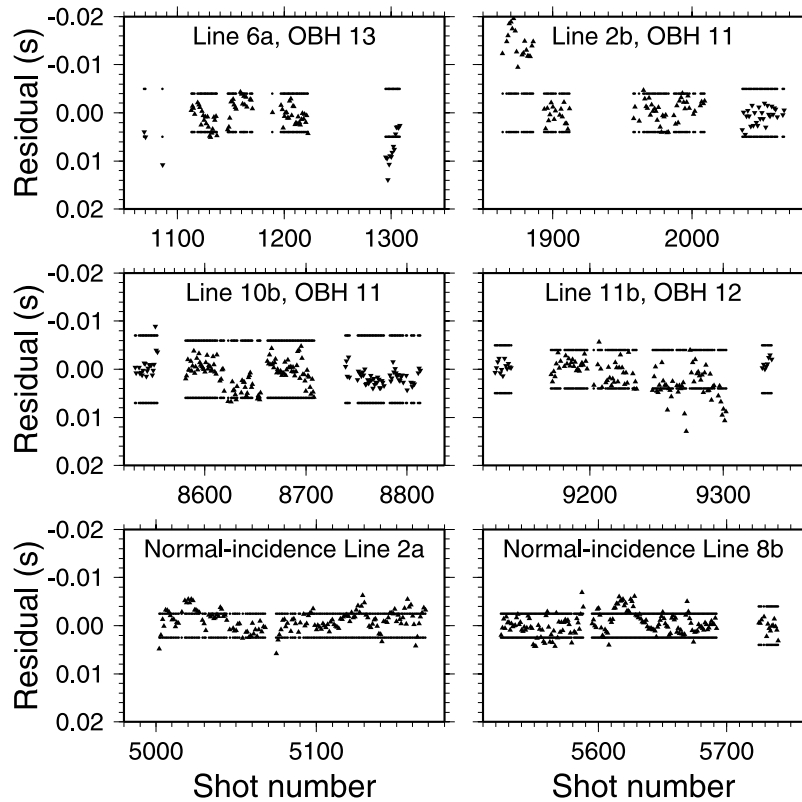


**Figure 5.** Typical residuals between observed and predicted travel times for the final model. Dots (which form broken horizontal lines) mark pick uncertainties, triangles mark residuals for BSR picks, and inverted triangles mark residuals for turning ray picks.

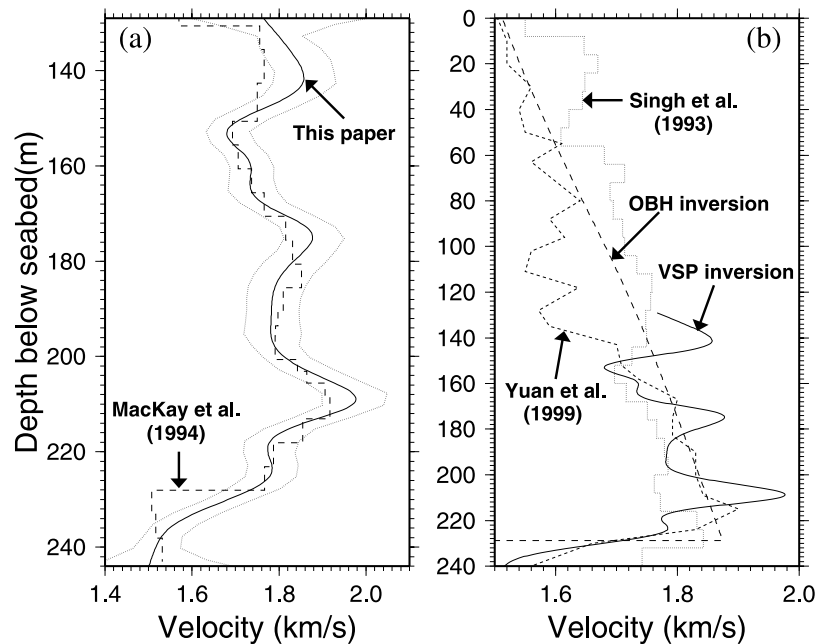


**Figure 6.** Velocity models at and close to ODP Site 889B. (a) Final result of VSP inversion (solid line), uncertainty bounds (dotted lines), and the result obtained by *MacKay et al.* [1994] (dashed line). (b) Result from VSP inversion (solid line), final result from OBH inversion (long-dashed line), result from waveform inversion of *Yuan et al.* [1999] (short-dashed line), and result from waveform inversion of *Singh et al.* [1993] (dotted line).

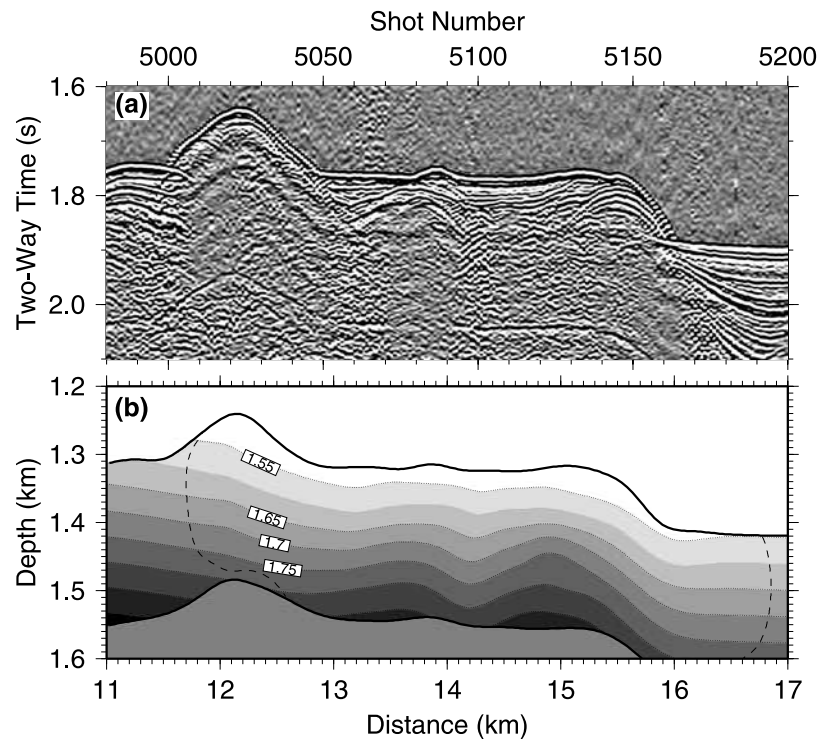


**Figure 7.** Comparison between (a) the deconvolved single channel reflection profile and (b) the final velocity model for line 2a. The dashed line marks the boundary of the well-constrained region of the velocity model (see text for discussion). The velocity structure close to the seabed follows the general trend of sedimentary reflectors, indicating that here velocities are controlled primarily by variations in porosity and lithology. Closer to the BSR this correlation is lost and velocities are likely controlled more by hydrate content.

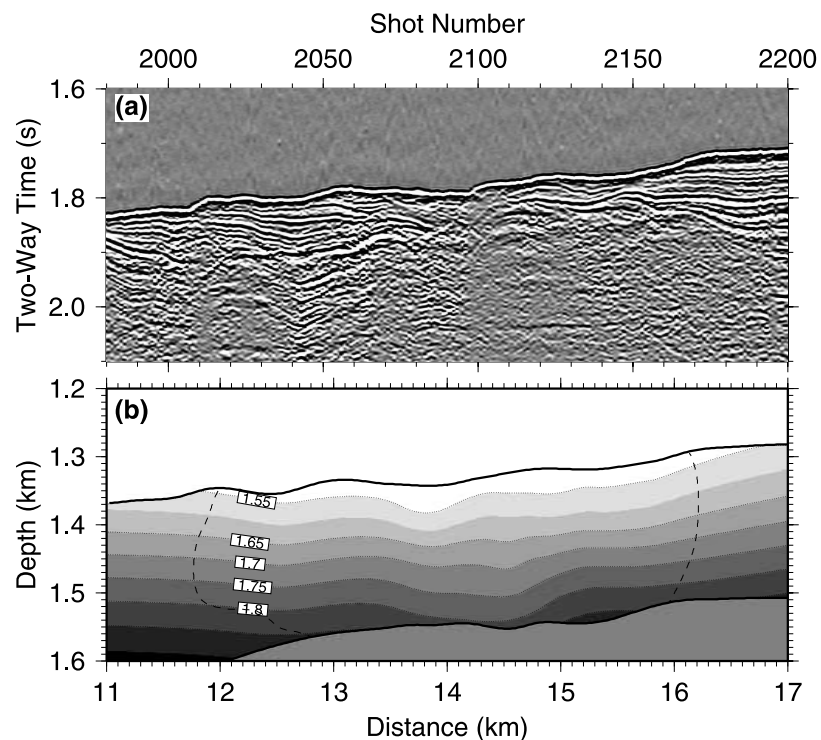


**Figure 8.** Comparison between (a) the deconvolved single channel reflection profile and (b) the final velocity model for line 7a, with the boundary of the well-constrained region as in Figure 7.

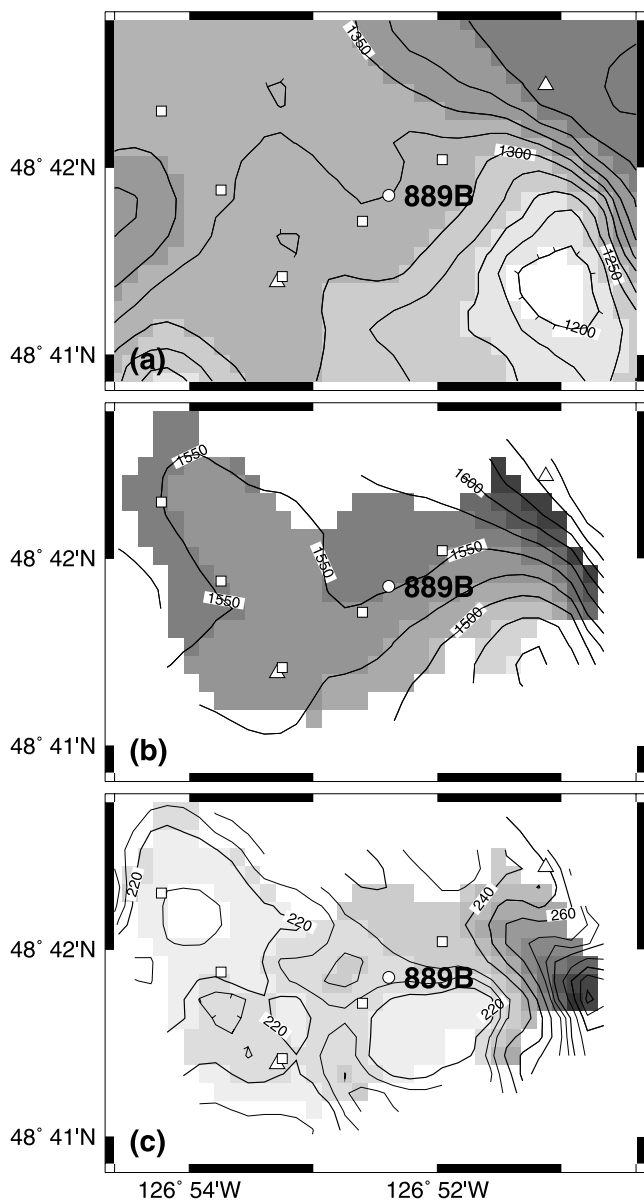


**Figure 9.** (a) Seafloor depth in the central part of the survey area. (b) BSR depth in the region where it is well-constrained (see text). (c) BSR depth below the seafloor in the region where it is well constrained. OBH positions and ODP Site 889 are marked as in Figure 1.

files. This correlation was maximized when the seabed model from deployment B was shifted 22.5 m to the south. This shift was applied to all shot positions from deployment B and then a combined inversion run using data from both deployments to determine the final seabed grid. This final grid matched 9952 picks, with a  $\chi^2$  value of 0.85. The final inverted water depth was compared to the relocated OBH positions: in all cases, the OBH depth was within 5 m of the seafloor depth. In a final adjustment for modeling wide-angle data, all OBHs were placed at their correct location 3 m above the seafloor. Our inversion provides accurate depths along the seismic lines and smooth bathymetry between them, which are necessary starting points for tomographic inversion of the subsurface phases.

[10] In the next step, we inverted for the velocity structure above the BSR. Three subsurface phases were picked that could be traced consistently in OBH data across the whole survey area: the BSR, turning energy above the BSR, and turning energy that formed first arrivals. The BSR was also picked in the coincident normal incidence reflection profiles. Pick uncertainties ranged from 4 ms to 20 ms depending on signal-to-noise ratio [Hobro *et al.*, 2003]. The point at which the BSR wide-angle reflection became a refraction just above the BSR was difficult to determine from the OBH record sections, so picks in the region of uncertainty were assigned to both phases. In inversions for subsurface structure, the seabed structure and water column velocity were fixed, the subsurface velocity structure was parameterized as 10 km by 11 km by 600 m cuboid containing  $30 \times 30 \times 12$  velocity nodes, and the BSR was parameterized by a grid of  $30 \times 30$  depth nodes covering the same area (Figure 1).

[11] The first inversion run used only turning arrivals picked after the direct water wave, with a high regularization strength; this resulted in a model with a roughly constant subsurface velocity gradient of  $1.53 \text{ s}^{-1}$ . The second run used in addition first arrival picks, but failed to converge, perhaps because these arrivals turn below the BSR. Since the focus of our study was the velocity structure of the gas hydrate stability field, these first arrival turning ray picks were omitted in subsequent inversions. The third run used the velocity model from run 1 and the normal incidence BSR picks, and inverted for BSR depth only with velocities fixed. The fourth run used only BSR picks from the OBH data; at this stage long-range BSR picks that could not be matched were eliminated from the set of reflection picks and assigned uniquely to refracted arrivals. In the final two runs, all phases except first arrivals were used and both subsurface velocity structure and BSR depth were optimized in a joint inversion. The fifth run used the same grid as runs 1–4, while the final run used the same number of velocity and depth nodes but focused in a smaller, 7 km by 6 km area where the model was best constrained (Figure 1). The final model matched 89% of 12446 travel time picks with a  $\chi^2$  of 0.72, with most picks fitting within their uncertainties (Figure 5). Most of the picks that were not successfully matched were likely assigned to the wrong phase, as discussed above. The velocity models from runs 5 and 6 differed very little; the model from run 6 was slightly smoother, perhaps because the coarse parameterization of run 5 resulted in some artifacts.

[12] The inversion method also uses linear inverse theory to estimate the formal uncertainties of velocity and depth parameters using the diagonal elements of the inverse of the Hessian matrix [Hobro *et al.*, 2003]. For the data set analyzed here, these formal uncertainties were relatively large: generally greater than  $0.2 \text{ km s}^{-1}$  and as large as  $0.6 \text{ km s}^{-1}$  in apparently well-constrained regions of the model. The large uncertainties may partly arise from a conservative choice of pick uncertainties, which were probably closer to an absolute limit of error than to the one standard deviation error assumed in the formal inversion analysis. In addition, a synthetic test by Hobro *et al.* [2003] showed that formal uncertainties were systematically larger than actual discrepancies between the true model and the recovered final model, for a smooth true model. We infer that the formal uncertainties calculated in this way are a

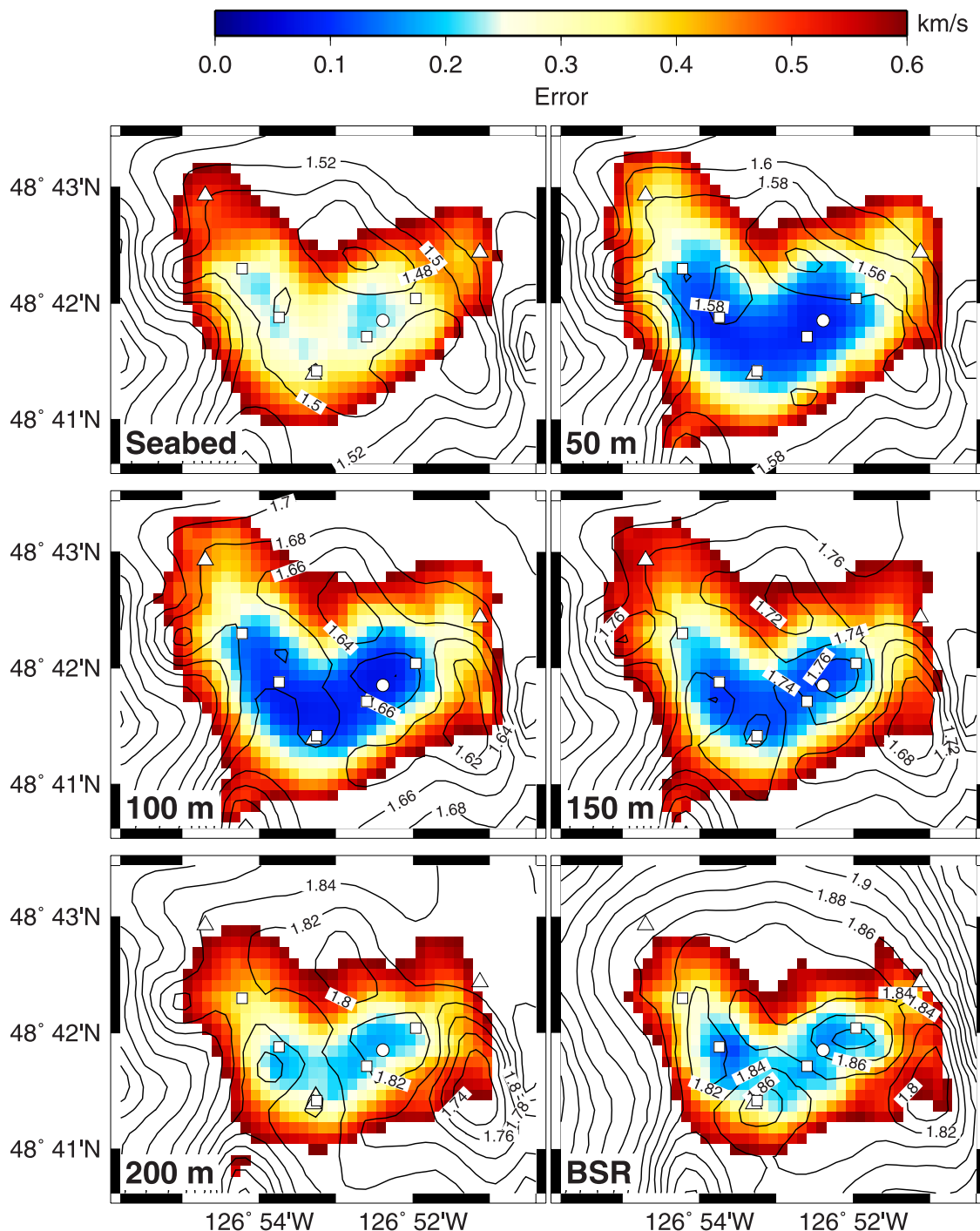


**Figure 10.** Representative slices through the final velocity model. Slices are shown at the seabed, at 50-m intervals through the hydrate stability zone and immediately above the BSR. Labeled contours mark velocities in  $\text{km s}^{-1}$ , and color scale marks the formal uncertainty from the inversion algorithm, which is likely overestimated by a factor of 2 or more (see text). The upper limit of the color scale marks the limit of the region which is considered to be well constrained (see text). OBH positions and ODP Site 889 are marked as in Figure 1.

good representation of relative uncertainties but a poor representation of their absolute values. In the discussion that follows, we use the  $0.6 \text{ km s}^{-1}$  uncertainty contour as a bound on the well-constrained region of the model, because the uncertainty increases steeply in the region of this

contour but is flatter within it. The discrepancy between the true velocity and the velocity recovered by the inversion within this region is probably less than half this value. Since BSR picks are densely spaced in the central part of our survey area, the BSR depth is considered well constrained

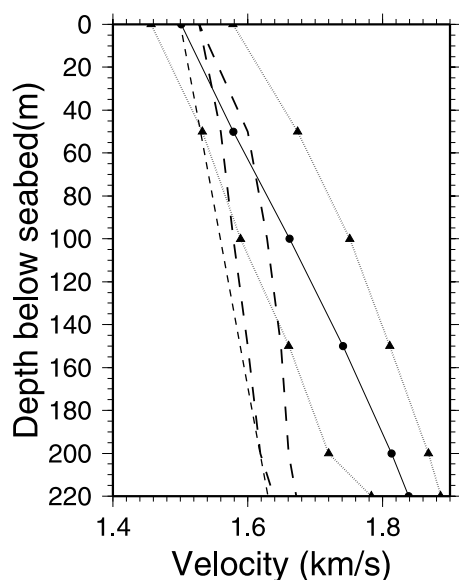


**Figure 11.** Mean velocity in the constrained region for each of the slices shown in Figure 10 (circles) and maximum and minimum velocity in the constrained region of each slice (triangles). Velocities at the BSR are plotted at a depth of 220 m below the seafloor. Short-dashed line marks no-hydrate reference curve of *Yuan et al.* [1996]. Long-dashed lines mark the velocity computed using the approach of *Jakobsen et al.* [2000] for the best fitting exponential porosity-depth relation (higher values) and the upper limit of porosity from the borehole porosity log at Site 889 (lower values).

where the velocity between the seabed and the BSR is well constrained.

## 5. Results and Discussion

[13] A useful test of the final three-dimensional model comes from an independent analysis of the vertical seismic profile (VSP) conducted at ODP Site 889. These data were originally analyzed by *MacKay et al.* [1994] using a linear regression approach. We repicked VSP travel times from the original seismograms and applied our inversion algorithm to these picks alone to determine a one-dimensional velocity model at the borehole, parameterized using 120 velocity nodes with a vertical spacing of 2.5 m. The inversion was allowed to proceed to a  $\chi^2$  value of 0.70 so that a reasonably abrupt velocity discontinuity at the BSR was developed. The final model is very similar to that of *MacKay et al.* [1994] but differs in detail, and the new inversion allows formal errors to be computed (Figure 6a). A vertical profile through the three-dimensional velocity model at the ODP site passes directly through the center of the VSP-derived velocities (Figure 6b), showing that at this location the tomographic model is a good, if low-pass-filtered, version of reality. Above the depths constrained by the VSP, velocities fall between those inferred from analyses of nearby multichannel seismic data by *Singh et al.* [1993] and by *Yuan et al.* [1999] (Figure 6b).

[14] Two perpendicular profiles through the best constrained regions of the model are shown in Figures 7 and 8.

On these profiles, it can be seen that there is a broad correlation between stratigraphic reflectors and velocity contours in the top  $\sim 100$  m below the seafloor, such that folded accreted sediments have slightly higher velocities at the same depth than the slope basin sediments that have accumulated in the anticlines of the folds. These differences may be attributed to compression-induced compaction and cementation [*Jarrard, 1997*]. At greater depths below the seafloor, this correlation is absent; here, the relatively high velocities suggest significant hydrate content. As expected, the BSR closely follows the seafloor (Figures 9a and 9b) and lies at  $220 \pm 10$  m below the seafloor across most of the  $\sim 6$  km<sup>2</sup> region where it is well constrained (Figure 9c). This observation suggests that the geothermal gradient, at the scale resolved by our model, varies little across this area. In general the BSR is smoother than the seabed, as is expected for isotherms, and this result is not an artifact of the regularization because the BSR picks are densely spaced and have small uncertainties.

[15] Within the well-constrained region of the model, velocity patterns vary little with depth below the seabed (Figure 10). This effect results partly from the fact that constraints come primarily from reflection picks with steep ray paths, so horizontal velocity variations are recovered with better resolution than vertical variations. The magnitude of velocity variations also varies little with depth, and the difference between maximum and minimum velocity is never as large as  $0.2$  km s<sup>-1</sup> within an individual depth slice (Figure 11). Porosity variations appear unlikely to be sufficient to explain the rapid increase in velocity with depth (Figure 11). The largest compositional effect on seismic velocity will come from variations in clay content, since clay minerals have much lower elastic moduli than the other major components of continental margin sediments. However, a 10% change in clay content is unlikely to result in a velocity change of more than  $50$  m s<sup>-1</sup> [see *Chand et al., 2004, Figure 3*], and there is no evidence for an increase in clay content with depth in our survey area (see below). Therefore, while variations in lithology and porosity no doubt contribute to the observed velocity variations, we expect the dominant contribution, particularly at depth, to come from variations in hydrate content.

[16] We determined hydrate content using the approach of *Jakobsen et al.* [2000], who used a combination of the self-consistent approximation (SCA) and differential effective medium theory (DEM). We used the full anisotropic method, but assumed that ellipsoidal clay particles have a uniform orientation distribution, so that the predicted velocities are isotropic. A variety of different effective medium methods have been applied in the literature, but all give broadly similar results [*Chand et al., 2004*] if the same microstructure is assumed. The SCA/DEM approach used requires the mineralogy and porosity to be specified. Grain size analyses of material from Site 889 suggested 50–60% clay fraction in the top 50 m, increasing to 70–75% at 130 m depth and falling again to  $\sim 50\%$  close to the BSR [*Camerlenghi et al., 1995*]. However, a high proportion of the clay size fraction appears to consist of angular rock and mineral fragments rather than clay minerals [*Clennell and Maltman, 1995*]. On the basis of XRD and XRF analyses, *Kopf et al.* [1995] suggest that clay minerals do not exceed 35% by volume, with 15–20% quartz and the remaining

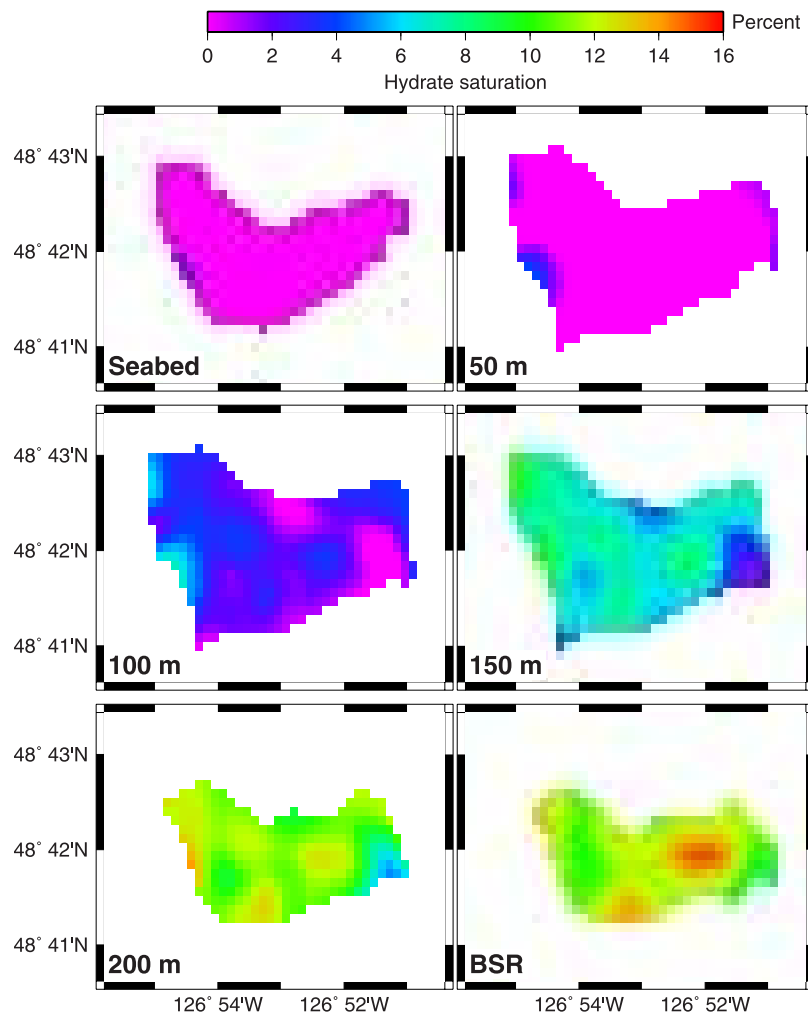


**Figure 12.** Hydrate content inferred for the depth slices of Figure 10, using the effective medium modeling approach of *Jakobsen et al.* [2000] (see text). The slice corresponding to velocities at the BSR is modeled using a porosity corresponding to 220 m depth below the seabed.

fraction consisting of mainly plagioclase feldspar with minor mica and calcite. We assumed in our analysis an average mineralogy of 35% clay, 20% quartz and 45% feldspar; the results are insensitive to small changes in these numbers. We used mineral, water and hydrate elastic moduli and densities as given by *Chand et al.* [2004], with values for feldspar of 37.5 GPa for the bulk modulus, 15.0 GPa for the shear modulus and  $2620 \text{ kg m}^{-3}$  for the density [*Mavko et al.*, 1998].

[17] On the basis of neutron logs, the porosity at Site 889 decreases from  $\sim 70\%$  at the seabed to  $\sim 52\%$  at the BSR [*Jarrard et al.*, 1995]. Piston core samples from the same general area also indicate a surface porosity of  $\sim 70\%$  [*Riedel et al.*, 2005]. We used an exponential porosity decay with parameters fit by regression to the log porosities. For comparison, we also estimated upper limiting porosities at the depths sampled by the velocity slices of Figure 10. In reality porosities at shallow depth may be overestimated rather than underestimated by our exponential fit, since piston core samples indicate very rapid compaction in the top few meters below the seabed [*Riedel et al.*, 2005].

[18] To compute  $P$  wave velocities in the absence of hydrate, we used the SCA for a clay-water composite as the

starting model, with other minerals added subsequently as inclusions. For both porosity models, the velocity predicted by the effective medium approach is higher than that of the polynomial no-hydrate reference curve of *Yuan et al.* [1996], though if the higher porosities are used the predicted velocity differs little from *Yuan et al.*'s curve, particularly at depth (Figure 11). Beyond  $\sim 140$  m depth, the minimum velocity within the well-constrained region is above the predicted velocity in the absence of hydrate. At shallower depths, however, velocities are observed that are lower than those predicted using the exponential porosity fit, and in the uppermost  $\sim 70$  m even the mean velocity is lower. These negative velocity anomalies may be due in part to errors in the velocity model. However, the error in the mean velocity is probably small, so limitations in the effective medium approach and deviations from the assumed porosity and mineralogy likely also contribute.

[19] To derive hydrate saturations from  $P$  wave velocities using the SCA approach, the SCA starting model must first be established. In the clay-rich Blake Ridge sediment at ODP Site 995, *Jakobsen et al.* [2000] concluded that a clay-water composite was the appropriate starting model, suggesting that hydrate lies primarily within the pore space.

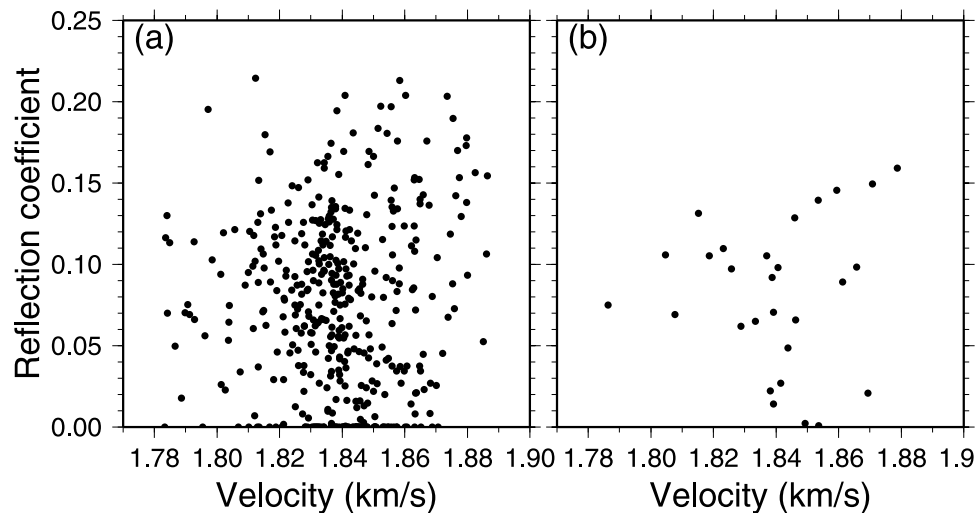


**Figure 13.** (a) BSR reflection coefficient as a function of the velocity immediately above the BSR, for the region where both are well constrained. Reflection coefficients are taken from *Fink and Spence* [1999], and the velocity grid was resampled at the interval of their reflection coefficient grid. (b) Same data resampled on a 500 m grid that is more representative of the horizontal resolution of the velocity model.

However, using higher estimates of clay content published after Jakobsen et al.'s work, *Chand et al.* [2004] could only reproduce the 10–20% hydrate saturations estimated from downhole resistivity logs by using a clay-hydrate composite as the SCA starting model, suggesting some degree of cementation at grain contacts. A recent laboratory study of hydrate formation in dry sand also favored hydrate cementation at grain contacts at saturations above 3–5% [*Priest et al.*, 2005]. Our results do not have the pore-scale resolution necessary to distinguish between these two end-member hydrate distributions. Instead, we computed velocity as a function of hydrate content by linearly mixing these two models such that the clay-water model contributes 100% of the result at 0% hydrate content and the clay-hydrate model contributes 100% of the result at 100% hydrate saturation. Estimated hydrate saturations increase systematically with depth from 0–4% at the seabed to 10–15% in the vicinity of the BSR (Figure 12). Saturations are increased by a factor of up to 1.04 if the highest porosities are used instead of the exponential fit. On the basis of the analysis of *Chand et al.* [2004], an error of 10% in the assumed clay content would result in an error of  $\sim 5\%$  in hydrate saturation, as would an error of  $100 \text{ m s}^{-1}$  in the velocity.

[20] It should be emphasized that our seismic data and our inversion approach resolve only broad-scale variations in hydrate content; smaller-scale variations both laterally [e.g., *Wood et al.*, 2002] and vertically [e.g., *Tréhu et al.*, 2004] are likely to be present, and much higher saturations may be locally present close to the seafloor [*Riedel et al.*, 2005]. The hydrate content at the scale of our sampling is not in any obvious way controlled by local bathymetry or structure, which is fairly flat in the well-constrained region (Figure 9). Perhaps it is controlled more by the channelized fluid flow inferred from higher-resolution seismic data [*Wood et al.*, 2002; *Riedel et al.*, 2002]. The mean calculated hydrate saturation is 0.1% at the seafloor, increasing to

2.4% at 100 m depth and 11.8% at the BSR, and the overall mean hydrate saturation within the constrained volume is 2.2% of the pore space, or 1.1% of the sediment volume. Our maximum values are somewhat lower than the 20–30% previously predicted for the vicinity of Site 889 based on downhole velocity and borehole resistivity measurements and a more empirical approach [*Hyndman et al.*, 2001].

[21] The velocity model, combined with the reflection coefficient data set derived by *Fink and Spence* [1999], allows us to address directly the issue of the contribution of velocity increases due to hydrate content to the reflection coefficient of the BSR, as represented by the velocity immediately above the BSR. An initial comparison based on the data set presented by *Fink and Spence* [1999], who used a  $\sim 200\text{-m}$  grid, shows poor correlation between these two parameters (Figure 13a). However, this comparison does not account for navigational uncertainties, which are corrected in the velocity model but remain in the reflection coefficient grid. Such uncertainties may mean that the two grids are not properly registered. In addition, the regularization eliminates short-wavelength horizontal velocity variations in the tomographic model. Horizontal velocity variations with wavelengths of  $\sim 500 \text{ m}$  and greater appear to be recovered by the inversion (e.g., Figures 7 and 8). Therefore we made a second comparison by resampling both velocity and reflection coefficient data onto a 500 m grid. There remains no correlation between the velocity immediately above the BSR and the BSR reflection coefficient (Figure 13b).

[22] We conclude therefore that the BSR reflection coefficient is controlled primarily by the properties of the region of free gas immediately beneath the BSR. Using both velocity and reflection coefficient data sets, the seismic velocity beneath the BSR may be inferred if it is assumed to be thick enough for thin layer tuning effects to be unimportant, and that the density does not change significantly across the BSR. The latter assumption is reasonable

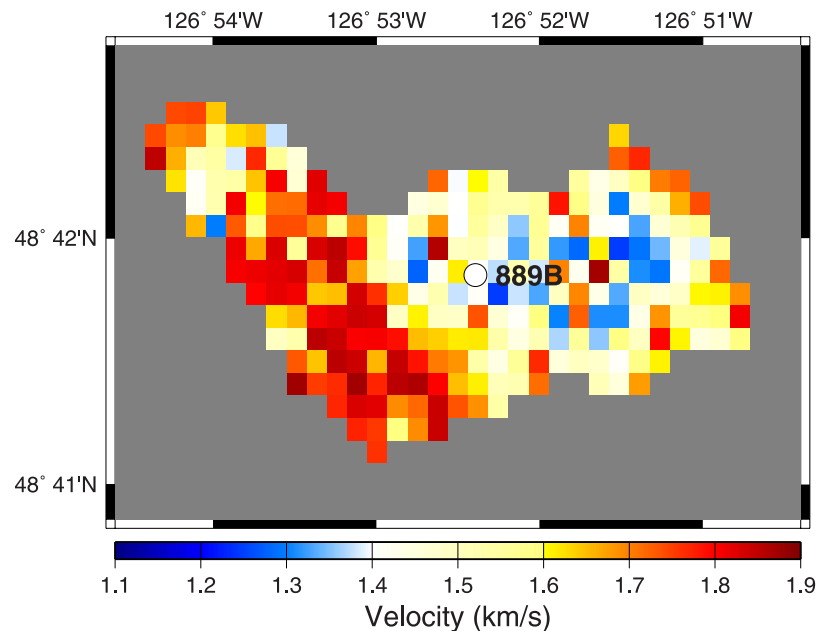


**Figure 14.** Seismic velocity immediately beneath the BSR, inferred from the reflection coefficient grid of *Fink and Spence* [1999] and the velocity immediately above the BSR from tomographic inversion, assuming that there is no density contrast at the BSR.

since both hydrate and gas lower the overall sediment density but may fail if large amounts of gas are present, since the density of gas is somewhat lower than that of hydrate. Such a calculation suggests a velocity immediately beneath the BSR ranging from 1.17 to 1.88 km s<sup>-1</sup>, with a mean of 1.60 km s<sup>-1</sup> (Figure 14). In reality, thin layer tuning effects are likely to be important [e.g., *Singh et al.*, 1993], and the BSR has complex, fine-scale structure [*Wood et al.*, 2002]. In this case the lower velocities may correspond to regions where the gas layer is sufficiently thick that the positive impedance contrast at its base does not affect the measured reflection coefficient, and the higher velocities to regions where the gas layer is thin and there is a degree of destructive interference. The relatively high mean value suggests that in general either the gas saturation is very low, or there is significant destructive interference, with the gas layer thinner than a quarter of the 15–20 m dominant wavelength of the seismic source and much thinner than the ~30 m determined close to Site 889 by *Singh et al.* [1993].

## 6. Conclusions

[23] From our three-dimensional seismic study of the gas hydrate stability zone around ODP Site 889, we make the following conclusions:

[24] 1. Seismic velocities within 50–100 m of the seabed in our survey area are controlled mainly by porosity and lithology; velocities between this region and the BSR are controlled mainly by hydrate content.

[25] 2. On the basis of effective medium theory calculations, the hydrate saturation increases with depth to a maximum of ~15% in the vicinity of the BSR, with an overall mean hydrate saturation of 2% within the volume where velocities are well constrained.

[26] 3. There is no correlation between the seismic velocity above the BSR and the BSR reflection coefficient, so the reflection coefficient is controlled primarily by the seismic velocity and/or thickness of the underlying gas layer, which is thin and/or has very low gas saturations.

[27] **Acknowledgments.** Data acquisition was funded by NSERC in Canada and NERC in the U.K. and was led by George Spence (University of Victoria). J.W.D.H. was supported by a NERC research studentship, and T.A.M. was partially supported by a Royal Society University Research Fellowship. We thank the officers, crew, and scientific party aboard R/V *John P. Tully* for their support at sea. We thank reviewers Warren Wood, Stefan Bünz, and William Waite for their constructive comments.

## References

- Camerlenghi, A., R. G. Lucchi, and R. G. Rothwell (1995), Grain size analysis and distribution in Cascadia margin sediments, northeastern Pacific, *Proc. Ocean Drill. Program Sci. Results*, 146, 3–31.
- Chand, S., T. A. Minshull, D. Gei, and J. Carcione (2004), Elastic velocity models for gas-hydrate-bearing sediments—A comparison, *Geophys. J. Int.*, 159, 573–590.
- Chapman, N. R., J. F. Gettrust, R. Walia, D. Hannay, G. D. Spence, W. T. Wood, and R. D. Hyndman (2002), High-resolution, deep-towed, multi-channel survey of deep-sea gas hydrate off western Canada, *Geophysics*, 67, 1038–1047.
- Clennell, B., and A. Maltman (1995), Microstructures in accreted sediments of the Cascadia margin, *Proc. Ocean Drill. Program Sci. Results*, 146, 201–209.
- Ecker, C., J. Dvorkin, and A. Nur (2000), Estimating the amount of gas hydrate and free gas from marine seismic data, *Geophysics*, 65, 565–573.
- Fink, C. R., and G. D. Spence (1999), Hydrate distribution off Vancouver Island from multifrequency single channel reflection data, *J. Geophys. Res.*, 104, 2909–2922.
- Hobro, J. W. D. (1999), Three-dimensional tomographic inversion of seismic travel-time data, Ph.D. dissertation, Univ. of Cambridge, Cambridge, U.K.
- Hobro, J. W. D., T. A. Minshull, and S. C. Singh (1998), Tomographic seismic studies of the methane hydrate stability zone in the Cascadia margin, in *Gas Hydrates*, edited by J.-P. Henriot and J. Mienert, *Geol. Soc. Spec. Publ.*, 137, 133–140.
- Hobro, J. W. D., S. C. Singh, and T. A. Minshull (2003), Three-dimensional tomographic inversion of combined reflection and refraction seismic traveltimes data, *Geophys. J. Int.*, 152, 79–93.

- Hyndman, R. D., and G. D. Spence (1992), A seismic study of methane hydrate marine bottom simulating reflectors, *J. Geophys. Res.*, *97*, 6683–6698.
- Hyndman, R. D., G. D. Spence, R. Chapman, M. Riedel, and R. N. Edwards (2001), Geophysical studies of marine gas hydrate in Northern Cascadia, in *Natural Gas Hydrates: Occurrence, Distribution and Detection*, *Geophys. Monogr. Ser.*, vol. 124, edited by C. K. Paull and W. P. Dillon, pp. 273–295, AGU, Washington, D. C.
- Jakobsen, M., J. A. Hudson, T. A. Minshull, and S. C. Singh (2000), Elastic properties of hydrate-bearing sediments using effective medium theory, *J. Geophys. Res.*, *105*, 561–577.
- Jarrard, R. D. (1997), Origins of porosity and velocity variations at Cascadia accretionary prism, *Geophys. Res. Lett.*, *24*, 325–328.
- Jarrard, R. D., M. E. MacKay, G. K. Westbrook, and E. J. Screaton (1995), Log-based porosity of ODP sites on the Cascadia accretionary prism, *Proc. Ocean Drill. Program Sci. Results*, *146*, 313–335.
- Katzman, R., W. S. Holbrook, and C. K. Paull (1994), Combined vertical-incidence and wide-angle seismic study of a gas hydrate zone, Blake Ridge, *J. Geophys. Res.*, *99*, 17,975–17,995.
- Kopf, A., J. C. Sample, P. Bauer, J. H. Behrmann, and H. Erlenkeuser (1995), Diagenetic carbonates from Cascadia margin: Textures, chemical compositions, and oxygen and carbon stable isotope signatures, *Proc. Ocean Drill. Program Sci. Results*, *146*, 117–136.
- Korenaga, J., W. S. Holbrook, S. C. Singh, and T. A. Minshull (1997), Natural gas hydrates on the southeast U.S. margin: Constraints from full waveform and traveltimes inversions of wide-angle seismic data, *J. Geophys. Res.*, *102*, 15,345–15,365.
- Lee, M. W., D. R. Hutchinson, T. S. Collett, and W. P. Dillon (1996), Seismic velocities for hydrate-bearing sediments using weighted equation, *J. Geophys. Res.*, *101*, 20,347–20,358.
- MacKay, M. E., R. D. Jarrard, G. K. Westbrook, R. D. Hyndman, and the Shipboard Scientific Party of ODP Leg 146 (1994), Origin of bottom simulating reflectors: Geophysical evidence from the Cascadia accretionary prism, *Geology*, *22*, 459–462.
- Mavko, G. T., T. Mukerji, and J. Dvorkin (1998), *The Rock Physics Handbook—Tools for Seismic Analysis in Porous Media*, Cambridge Univ. Press, New York.
- Priest, J. A., A. I. Best, and C. R. I. Clayton (2005), A laboratory investigation into the seismic velocities of methane gas hydrate-bearing sand, *J. Geophys. Res.*, *110*, B04102, doi:10.1029/2004JB003259.
- Riedel, M., G. D. Spence, N. R. Chapman, and R. D. Hyndman (2002), Seismic investigations of a vent field associated with gas hydrates, offshore Vancouver Island, *J. Geophys. Res.*, *107*(B9), 2200, doi:10.1029/2001JB000269.
- Riedel, M., I. Novosel, G. D. Spence, R. D. Hyndman, R. N. Chapman, R. C. Solem, T. Lewis, and L. Zuelsdorff (2005), Geophysical and geochemical signatures associated with gas hydrate related venting at the north Cascadia margin, *Geol. Soc. Am. Bull.*, in press.
- Singh, S. C., T. A. Minshull, and G. D. Spence (1993), Velocity structure of a gas hydrate reflector, *Science*, *260*, 204–207.
- Spence, G. D., T. A. Minshull, and C. Fink (1995), Seismic studies of methane gas hydrate, offshore Vancouver Island, *Proc. Ocean Drill. Program, Sci. Results*, *146*(Part 1), 163–174.
- Tréhu, A. M., et al. (2004), Three-dimensional distribution of gas hydrate beneath southern Hydrate Ridge: Constraints from ODP Leg 204, *Earth Planet. Sci. Lett.*, *222*, 845–862.
- Westbrook, G. K., et al. (1994), *Proceedings of the Ocean Drilling Program, Initial Reports*, vol. 146, Part 1, Ocean Drill. Program, College Station, Tex.
- Wood, W. T., J. F. Gettrust, N. R. Chapman, G. D. Spence, and R. D. Hyndman (2002), Decreased stability of methane hydrates in marine sediments owing to phase-boundary roughness, *Nature*, *420*, 656–660.
- Yuan, J., and R. N. Edwards (2000), The assessment of marine gas hydrates through electrical remote sounding: Hydrate without a BSR?, *Geophys. Res. Lett.*, *27*, 2397–2400.
- Yuan, T., R. D. Hyndman, G. D. Spence, and B. Desmons (1996), Seismic velocity increase and deep-sea gas hydrate concentration above a bottom-simulating reflector on the northern Cascadia continental slope, *J. Geophys. Res.*, *101*, 13,665–13,671.
- Yuan, T., G. D. Spence, R. D. Hyndman, T. A. Minshull, and S. C. Singh (1999), Seismic velocity studies of a gas hydrate bottom simulating reflector on the northern Cascadia continental margin: Amplitude modeling and full waveform inversion, *J. Geophys. Res.*, *104*, 1179–1191.
- Zühlsdorff, L., and V. Spiess (2004), Three-dimensional seismic characterization of a venting site reveals compelling indications of natural hydraulic fracturing, *Geology*, *32*, 101–104.

S. Chand, Geological Survey of Norway, Tromsøkontoret, Polarmiljø-senteret, NO-9296 Tromsø, Norway. (shyam.chand@ngu.no)

J. W. D. Hobro, WesternGeco, Schlumberger House, Buckingham Gate, Gatwick Airport RH6 0NZ, UK. (jhobro@slb.com)

T. A. Minshull, Southampton Oceanography Centre, Southampton SO14 3ZH, UK. (tmin@soc.soton.ac.uk)

S. C. Singh, Laboratoire de Géosciences Marines, Institut de Physique du Globe de Paris, 4 Place Jussieu, F-75252 Paris Cedex 05, France. (singh@ipgp.jussieu.fr)